# 3.5 Damping Ring

## 3.5.1 Introduction

The normalized transverse emittance of the beam produced at the positron source is several orders of magnitude larger than the design emittance for collider operation. The only conceivable way to achieve the required emittance is to store the beam temporarily (between linac pulses) in a damping ring. In case of the electron beam, using a laser rf-gun may be a way to produce a beam with sufficiently small emittances. This could provide a cost saving first stage of TESLA with only one damping ring. However, for optimum performance of the collider with a vertical emittance as small as possible, an electron damping ring will likely be required as well. Since there are only minor differences between the electron and the positron version of the damping ring, with somewhat relaxed requirements for the e- ring, we focus in this section on the positron ring design.

Assuming a normalised emittance of the positron beam injected into the ring of $\gamma\epsilon_i = 0.01\,\mathrm{m}$ (see section 3.4.5), the required emittance reduction factors are $\epsilon_{f;x}/\epsilon_i = 1.2\times10^{-3}$ and $\epsilon_{f;y}/\epsilon_i = 2\times10^{-5}$ for the horizontal and vertical plane, respectively. Here, a 25 % emittance dilution budget between extraction from the ring and the interaction point is included. The final emittance in the ring after a storage time equal to the linac cycle time $T_c = 200\,\mathrm{ms}$ is given by

$$\epsilon_f = \epsilon_{eq} + (\epsilon_i - \epsilon_{eq})exp(-2T_c/\tau_D) \tag{3.5.1}$$

where $\epsilon_{eq}$ and $\tau_D$ denote the equilibrium emittance and transverse damping time, respectively. The resulting requirements for these basic parameters are summarized in table 3.5.1.

In order to keep the demands for the bunch compressor moderate, the damping ring should also fulfill limitations concerning the longitudinal phase space. Furthermore, the ring must safely accomodate the injected positron beam, which sets lower limits on the transverse and longitudinal acceptance. These additional parameters are included in table 3.5.1.

The main complication which arises for the TESLA damping ring design is due to the pulse structure of the linac. The train of 1130 bunches per pulse has a length of 0.8 ms, or 240 km. Since a damping ring of that size would be unreasonable, the bunchtrain must be stored in the ring in a compressed mode, with a bunch spacing much smaller than in the linac. The bandwidth of the systems required for injection into and extraction from the ring are inversely proportional to the bunchspacing in the ring. Furthermore, the demands for the fast multibunch feedback system grow with decreasing ring length. We choose here a ring design with a circumference of C=17 km, leading to rather conservative bandwidth requirements with a bunch spacing of 50 ns.

In the next subsection the general layout, the magnet lattice and the beam optics of the positron damping ring are discussed. It is followed by descriptions of the injection/extraction devices, the vacuum system and the rf-system. Furthermore an analysis of collective beam dynamics and of requirements for feedback systems is given.

| | |
|---|---|
| $e^+$ emittance at injection $\gamma\epsilon_{i;x,y}$ | $0.01m$ |
| hor. equilibrium emittance $\gamma\epsilon_{eq;x}$ | $1.2 \times 10^{-5}m$ |
| hor. emittance at extraction $\gamma\epsilon_{f;x}$ | $1.2 \times 10^{-5}m$ |
| vert. equilibrium emittance $\gamma\epsilon_{eq;y}$ | $1.0 \times 10^{-7}m$ |
| vert. emittance at extraction$\gamma\epsilon_{f;y}$ | $2.0 \times 10^{-7}m$ |
| cycle time $T_c$ | $200ms$ |
| transverse damping time $\tau_{D;x,y}$ | $35ms$ |
| equilibrium bunch length $\sigma_z$ | $< 1cm$ |
| equilibrium momentum spread $\sigma_p/p$ | $0.1\%$ |
| transverse acceptance $\gamma A_{x,y}$ | $> 0.05m$ |
| momentum acceptance $A_p$ | $> 0.5\%$ |

Table 3.5.1: *Goal parameters for the positron damping ring*

### 3.5.2 General Layout

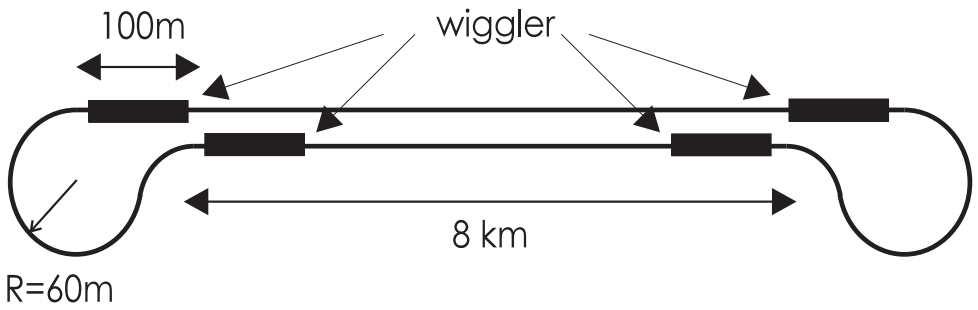


Figure 3.5.1: *General layout of the "dogbone"-shaped damping ring*

In order to avoid the need for a costly additional 17 km ring tunnel, the TESLA damping ring is designed such that about 95 % of the lattice can be installed in the linac tunnel. Additional tunnels are only required for the two "loops" at the ends of the 8 km long straight sections (see fig. 3.5.1). The geometry of these arcs is shown in more detail in fig. 3.5.2. They consist of a negative bending section with a bend angle of $\Phi_- = -11/48 \times 2\pi$, followed by a short straight section and a positive bending section with $\Phi_+ = 35/48 \times 2\pi$. The length of the straight section is adjusted such that a horizontal spacing of the long straight sections in the linac tunnel of 0.8 m results. The basic unit of the arcs is a FODO cell with a bend angle of $\pi/24$ and an average bending radius of 60m (the negative and positive bending sections have 11 and 35 FODO cells, respectively). In order to achieve a sufficiently small damping time, wiggler sections are foreseen at the end of the long straights (fig. 3.5.1). The transverse damping time can be written as (partition numbers $J_{x,y} = 1$)

$$\tau_{x,y} = \frac{2E_b C}{U_0 c} \tag{3.5.2}$$

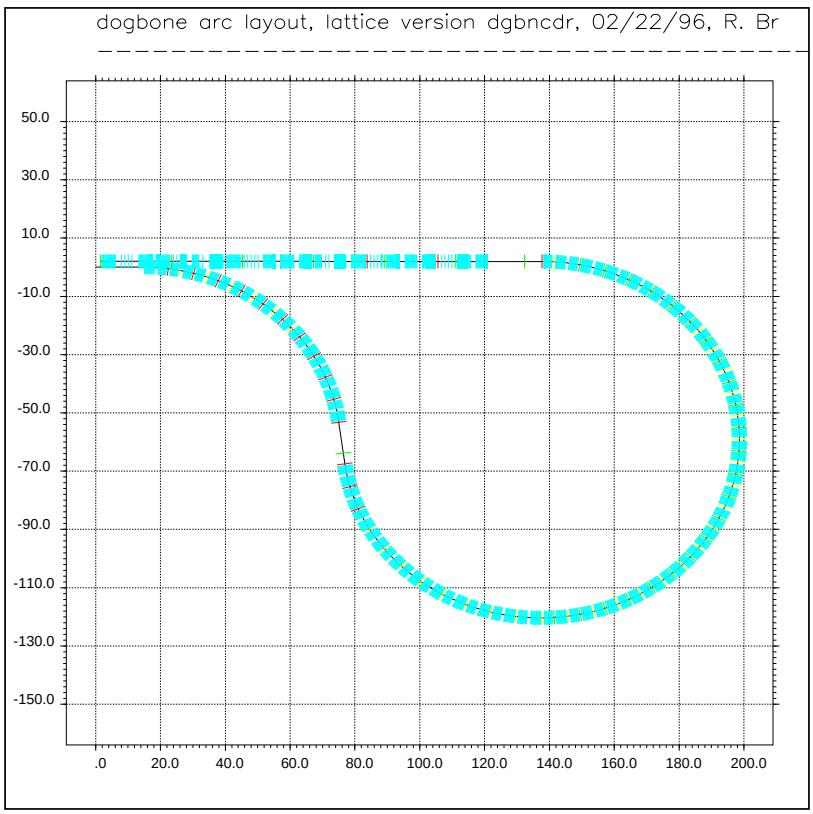


Figure 3.5.2: *Geometry of the "dogbone" damping ring arcs*

where $E_b$ is the beam energy and $U_0$ the energy loss per revolution. The latter is given by

$$U_0[MeV] = 1.26 \cdot 10^{-3} \times E_b^2 \oint B^2 ds \tag{3.5.3}$$

with $E_b$ in GeV and the magnetic field $B$ in T. For the beam energy we choose $E_b = 3.2\,\mathrm{GeV}$ as the result of a parameter optimization, taking into account considerations such as:

- The RF-system. The required circumferential voltage $U_{RF}$ grows with increasing $E_b$.
- The emittance contribution from the arcs. For a given beam optics, the normalized horizontal emittance scales approximately as $\gamma\epsilon_{arc} \propto E_b^6$, when the dominant contribution to the damping comes from the wigglers.
- The bunch compressor, which favors a low beam energy.
- The total length $L_w$ of the wigglers. For given field strength $B$, $L_w$ scales like $E_b^{-1}$, thus favoring a high beam energy.

Using eqs. 3.5.2 and 3.5.3 yields for the required damping integral:

$$\oint B^2 ds \approx \int_{\text{wiggler}} B^2 ds = 805\ T^2 m \tag{3.5.4}$$

and for the energy loss per revolution

$$U_0 = 10.4\ MeV \tag{3.5.5}$$

The wiggler design described below has $B_w = 1.5\,\text{T}$, so that the length of each of the four wiggler sections is about 100 m. The relative beam energy spread $\sigma_E$ is determined from $E_b$ and $B_w$ as:

$$\sigma_E \approx 0.468 \cdot 10^{-3} \times \sqrt{E_b[\text{GeV}] B_w[\text{T}]} = 1.02 \cdot 10^{-3} \tag{3.5.6}$$

The roughly 8 km long straight sections are layed out as simple periodic FODO channels. Injection and extraction takes place at opposite ends of the straight section, so that the damping ring itself acts as part of the beamline required to transfer the positrons to the entrance of the main linac.

### 3.5.3 Beam Optics

Despite the somewhat unconventional layout of the "dogbone"-shaped damping ring, the beam-optical design is rather straight-forward and simple. In the following, the beam optics for the different parts of the ring are discussed. A compilation of the main parameters of the damping ring is given at the end of this section (table 3.5.6).

#### Straight Sections

The basic unit of the long straight sections is a 60° phase advance FODO cell of 100 m length. This choice of focussing strength is a compromise between keeping the $\beta$-functions within limits and avoiding an excessive contribution to the chromaticity, which can only be compensated in the relatively short arcs. For the quadrupoles, an aperture radius of 50 mm is foreseen, which provides a linear acceptance well in excess of the value required for the injected beam. The required gradient is small, so that a simple, low-cost design can be chosen (small amount of iron, no water cooling required). A summary of the beam optics and magnet parameters is given in table 3.5.2.

#### Arcs

The FODO cell in the arcs has a length of 8.5 m. Each cell comprises two quadrupoles, two dipoles, two sextupoles and two correction magnets. The design value of the phase advance is set to 90° per cell. The corresponding magnet strengths and optics parameters are listed in table 3.5.3. The quadrupoles and sextupoles are designed to allow for an increase in focussing strength, which provides sufficient flexibility to provide a smaller horizontal emittance and momentum compaction factor when desirable. In

| | |
|---|---|
| FODO cell length | 100 m |
| cell phase advance | 60° |
| total # of cells | 152 |
| chromaticity contribution $\xi_{x,y}$ | 27.9 |
| maximum $\beta_{x,y}$ | 175 m |
| average $\beta_{x,y}$ | 110 m |
| aperture radius | 50 mm |
| norm. linear acceptance | 0.089 m |
| quadrupole length | 0.2 m |
| quadrupole gradient | 1.05 $\mathrm{Tm}^{-1}$ |
| Ampère windings | 1000 |
| power per quad | 70 W |

Table 3.5.2: *Optics and magnet parameters for the straight sections*

| | |
|---|---|
| FODO cell length | 8.5 m |
| cell phase advance | 90° |
| total # of cells | 92 |
| chromaticity contribution $\xi_{x,y}$ | 29.3 |
| maximum $\beta_{x,y}$ | 13.5 m |
| average $\beta_{x,y}$ | 8.3 m |
| half aperture ($hor. \times vert.$) | 25×15 mm |
| norm. linear acceptance | 0.10 m |
| dipole length | 3 m |
| dipole field | 0.205 T |
| Ampère windings | 5720 |
| quadrupole length | 0.2 m |
| quadrupole gradient | 19.2 $\mathrm{Tm}^{-1}$ |
| Ampère windings | 4300 |
| power per quad | 1 kW |
| sextupole length | 0.2 m |
| sextupole gradient (max.) | 113 $\mathrm{Tm}^{-2}$ |

Table 3.5.3: *Optics and magnet parameters for the arc sections*

the design optics, the arc contribution to the normalized emittance amounts to $\gamma\Delta\epsilon_x = 0.23 \times 10^{-5}$ m (the main contribution comes from the wigglers, see below). The total natural chromaticity of the arcs is comparable to the one from the straights, but it has to be taken into account that the entire ring chromaticity must be compensated in the arcs in order to define the required sextupole strengths. All magnets have conservative strengths requirements and can be built as standard storage ring components (e.g. of the type used in the HERA electron ring, scaled down in size).

At the end of the arcs, a dispersion suppressor and matching section is foreseen adjacent to the wiggler sections. The matching between the positive and negative

bending sections in the arcs is provided by a "$-I$ transformer", see fig 3.5.3.

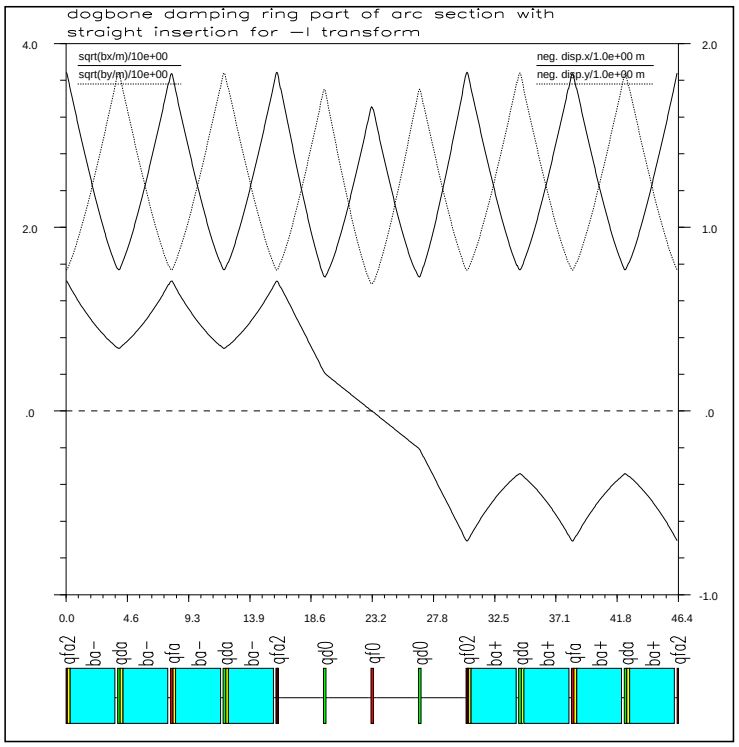


Figure 3.5.3: *Beam optics in the arc section showing the sign reversal of the dispersion function by inserting two "empty" FODO cells.*

### Wiggler Sections

Besides fulfilling the requirement for the damping integral, as described above, the wiggler section must be layed out such that the required horizontal emittance is safely achieved. For a wiggler with approximately rectangular field shape (period length $\lambda_w$ large compared to gap height $g_w$), the emittance is given by:

$$\gamma\epsilon_x = 2.22 \cdot 10^{-6} m \times B_w^3 \lambda_w^2 \beta_{x,w} \tag{3.5.7}$$

where $\beta_{x,w}$ denotes the horizontal beta function averaged over the wiggler length. With our choice $B_w = 1.5\,\mathrm{T}$ and $\lambda_w = 0.4\,\mathrm{m}$, we need $\beta_{x,w} \approx 10\,\mathrm{m}$. This requirement is easily met by arranging the lattice as a FODO structure with a cell length of about 10 m and a phase advance of 60°. The same quadrupoles as in the arcs can be used here. Sufficient reserve for the focussing strength is provided, thus allowing to reduce $\beta_{x,w}$ by about a factor of two if a smaller horizontal emittance is desirable. In total, 48 wiggler cells are installed, placed between the arcs and the long straight sections.

The contribution to the ring chromaticity (see table 3.5.4) is much smaller than from the long straight sections so that a tighter focussing in the wiggler cells will not have a large influence on the required sextupole strength in the arcs. Today wigglers and

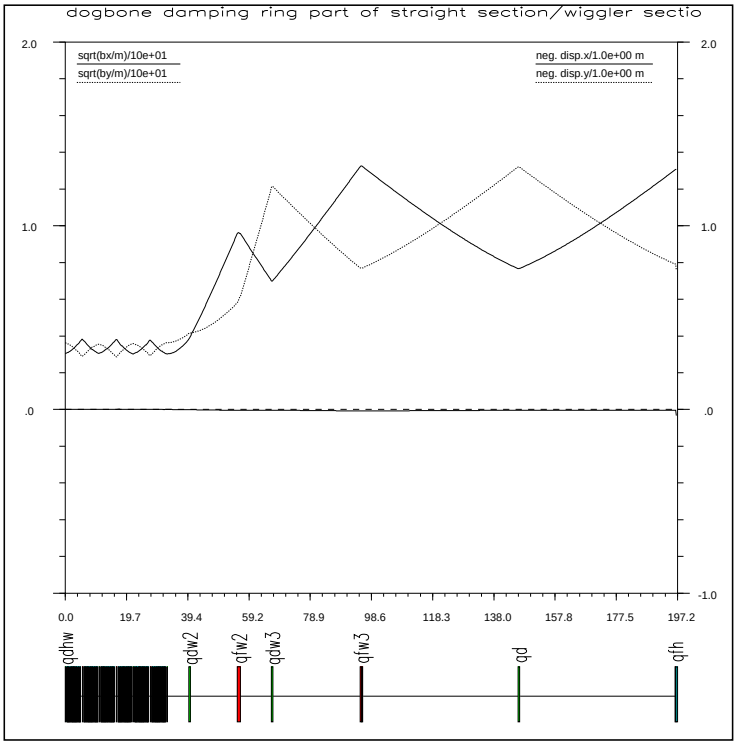


Figure 3.5.4: *Beam optics in the wiggler-to-straight matching section.*

undulators are widely used in both synchrotron radiation sources and Free Electron Lasers. During the last 15 years permanent magnet (PM) technology based initially on SmCo and later on NdFeB material has been developed to build these devices. At intermediate field levels up to about 2 T this technology is now almost exclusively used. The advantages of PM technology are evident: the devices are passive, which means they do not need any power supply, do not cause operational costs and require almost no maintenance. PM material is characterized by its $B-H$ demagnetization curve. The optimum operational point is chosen when the energy product $B \cdot H$ is maximum. In this case the volume of magnet material is minimized and given by :

$$V_m \simeq \frac{gh}{\mu_0 (BH)_{max}} \int B^2 dL, \tag{3.5.8}$$

The demagnetization curve of NdFeB is essentially a straight line throughout the second quadrant with a slope very close to one. In this case

$$(B \cdot H)_{max} \simeq \frac{1}{2} B_r \frac{1}{2} H_c \approx \frac{B_r^2}{4\mu_0}, \tag{3.5.9}$$

where $B_r$ is the remanent field, and $H_c$ is the coercive force of the material. Depending on material quality the maximum energy product for NdFeB is in the range of typically 240 – 340 kJ/m$^3$. Assuming 300 kJ/m$^3$ the absolute lower limit of material for the TESLA DR is about 2.8 m$^3$. A cross section of the wiggler aperture of $g \times w = 25 \times 50\,\mathrm{mm}^2$ is assumed here. Leakage flux and stray fields generally lead to larger volumes. We are using a wiggler design which has been optimized to have the point of operation close to the $(B \cdot H)_{max}$ value. The schematic layout of 1.5 T wiggler is shown in fig. 3.5.5. Conically shaped pole pieces are chosen which minimize leakage flux. A field distribution along the beam axis close to rectangular is produced. The effective fill factor is approximately given by $\eta_w = 1 - g_w/\lambda_w$ in order to account for the deviation from a rectangular field distribution in the transition between positive and negative field sections. This correction of about 7 % is included in the total wiggler length quoted in table 3.5.4.

| | |
|---|---|
| Damping integral $I_D$ | 815 T$^2$m |
| Wiggler length | 388 m |
| Fill factor | 93 % |
| # of wiggler units | 96 |
| Gap height $g_w$ | 25 mm |
| Period length $\lambda_w$ | 0.4 m |
| Peak field $B_w$ | 1.5 T |
| Volume of material | 4.8 m$^3$ |
| Required NeFeB | 36,000 kg |
| Chromaticity contribution $\xi_{x,y}$ | -4.8, -9 |
| norm. linear acceptance | 0.06 m |

Table 3.5.4: *Parameters of the wiggler section.*

### Tolerances and Correction Procedures

The vertical equilibrium emittance in the damping ring is essentially determined by the quadrupole, sextupole and BPM alignment tolerances and by the orbit correction procedures applied. We assume here tolerances as listed in table 3.5.5, which are close to state-of-the-art alignment accuracies achievable at installation time. The ring with errors has been simulated using the PETROS code. Standard orbit correction with the MICADO algorithm [1] is applied in several iterations, until the rms-orbit error does not improve significantly any more. This procedure is repeated for 25 different random seeds of errors. The typical residual rms-orbit deviation after correction is 0.30 mm. The resulting vertical beam emittance at extraction time is shown in fig.

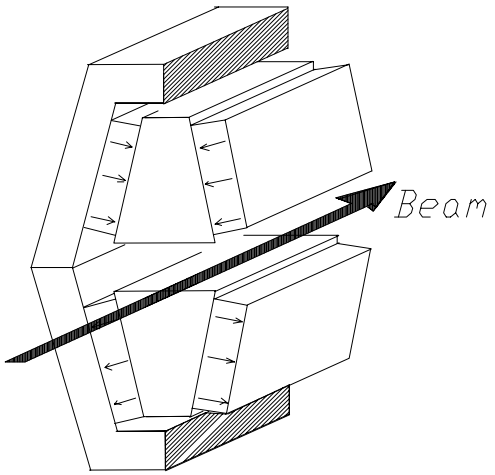


Figure 3.5.5: *Sketch of the 1.5T wiggler design.*

| Element | Error type | Tolerance (rms) |
|---|---|---|
| Quadrupoles (arcs) | Transverse position | 0.1 mm |
| (straight sections) | Transverse position | 0.2 mm |
| | Roll angle | 0.2 mrad |
| Sextupoles | Transverse position | 0.1 mm |
| | Roll angle | 0.5 mrad |
| Dipoles | Roll angle | 0.2 mrad |
| BPM's vs. quads | Transverse position | 0.1 mm |
| BPM resolution | Transverse position | 0.01 mm |

Table 3.5.5: *Alignment tolerances for the damping ring components.*

3.5.6. From the scattering of the simulation data, one can conclude that the design value of the emittance can be realistically achieved with just this standard method of orbit correction. By applying additional beam-based methods, it is possible to further reduce the vertical emittance. By improving the alignment of BPM's w.r.t. the focussing elements, a significant reduction of the spurious vertical dispersion can be achieved. This method has been applied at the HERA electron ring, in that case in context with spin polarization optimization [2]. Preliminary studies based on a BPM-alignment accuracy of 0.03 mm (rms) and the same orbit-kick minimization procedure used at HERA show that an equilibrium vertical emittance of $\gamma\epsilon_y \approx 2 \times 10^{-8}$ m is feasible. As an additional method, empirical emittance optimization using dispersive orbit bumps can be applied.

An important question concerns the long-term orbit stability and the typical time between necessary orbit corrections. From the experience at HERA [3], a diffusion-like orbit drift presumably caused by uncorrelated slow ground motion must be taken into account. From the HERA data we assume a ground motion according to the ATL-rule with $A \approx 10^{-5}\mu\mathrm{m}^2\mathrm{s}^{-1}$. This will cause a vertical emittance increase at a rate of $\gamma\Delta\epsilon_y/\Delta t \approx 2.5 \cdot 10^{-11}\mathrm{ms}^{-1}$. Steering the orbit back to the "golden" orbit every

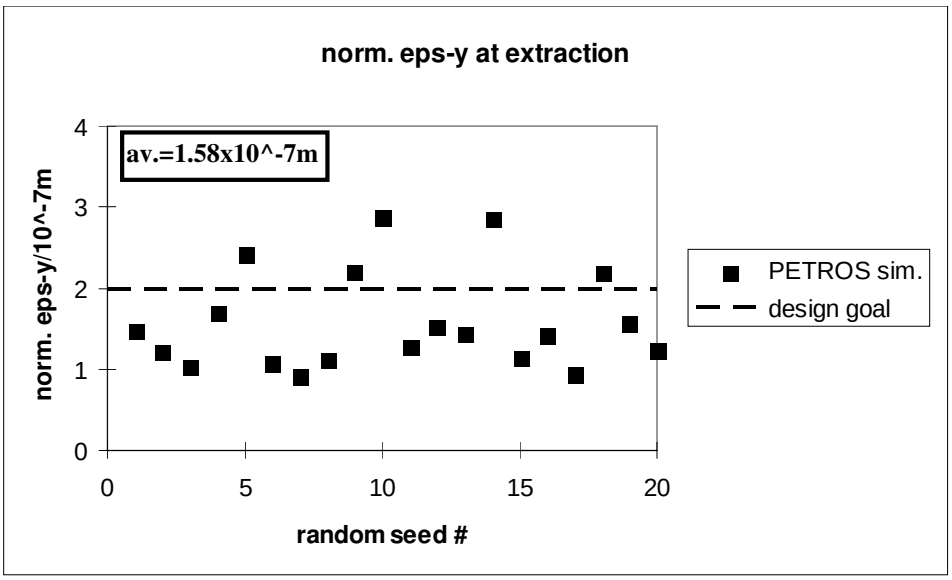


Figure 3.5.6: *Vertical emittance at extraction after applying orbit correction (see text). Results of PETROS simulations for 25 different random seeds of magnet position errors are shown. The dashed line denotes the design emittance according to table 3.5.1.*

20 min. will limit the relative emittance increase to about 4 %. This correction of an orbit change can be done at an accuracy limited only by the resolution of the BPM's, which is much better than their absolute alignment precision. In the HERA electron ring, the BPM resolution is about $20\mu$ m if the orbit is averaged over 64 revolutions. The goal of $10\mu$ m BPM resolution for the damping ring should be attainable without problems by longer averaging.

It can be concluded that from the point of view of beam optics and tolerances the design emittances in the damping ring can be safely achieved and that there is room for an improvement of the vertical emittance by about an order of magnitude.

### Beam-Gas and Intra-Beam Scattering

Incoherent scattering processes set upper limits on the beam lifetime and lower limits on the beam emittances in the damping ring. The dominant contribution to vertical emittance growth is due to elastic Coulomb scattering with the gas nuclei. The rms emittance growth from this effect is given by [4]:

$$\gamma\epsilon_{y,BG} = \frac{\pi c r_e^2}{\tau_y^{-1}\gamma} < \beta_y N_{gas} > l_{sc} \tag{3.5.10}$$

Here, $N_{gas}$ is the number density of gas molecules and $l_{sc}$ depends logarithmically on the ratio of maximum to minimum scattering angle ($l_{sc} \approx 5$). Due to the large beta-function, the vacuum pressure in the long straight sections is most critical. For $p_{gas} =$

$10^{-9}$ mbar in the straight sections and $p_{gas} = 10^{-8}$ mbar (with Z=7.3, assuming CO-molecules) in the arcs and wiggler sections, we find an emittance increase of 16 % w.r.t. the design value. The rms emittance according to eq. (3.5.10) strongly overestimates the actual effect on the core of the beam, because the distribution function resulting from a small number of scattering events is very different from Gaussian [5]. Therefore, the resulting luminosity loss from beam-gas scattering in the damping ring is practically negligible.

Intrabeam scattering (IBS) has an effect on both the transverse and longitudinal emittances and can be viewed as imposing a lower limit on the 6-dimensional phase space density in the bunch. The IBS-growth rates are estimated in an approximation given in [6]. For the design emittance values from table 3.5.1 we find: $\tau^{-1}_{\epsilon,IBS} = 0.6\,s^{-1}, \tau^{-1}_{x,IBS} = 2.2\,s^{-1}, \tau^{-1}_{y,IBS} = 0.3\,s^{-1}$. This yields an increase of the horizontal emittance by 7 %, whereas the effect in the longitudinal and vertical plane can be neglected. It becomes clear that the vertical emittance can be further reduced by a large factor before the IBS-limitation sets in, especially if such a machine parameter upgrade is connected with a reduction of bunch charge, as described in section 3.1.

The most important limitation of the beam lifetime at high particle densities in the bunch is due to the Touschek effect (see e.g. [7]). This lifetime turns out to be several hours, so that the Touschek-effect is not even a limitation to operating the ring in a storage-mode, as may be desirable for commissioning and machine study purposes.

### Dynamic Acceptance

The dynamic acceptance of the damping ring is investigated by particle tracking using the RACETRACK simulation code. The sextupole strengths in the arcs are adjusted for zero chromaticites. Random offsets of the sextupoles w.r.t. the beam orbit, the dominant source of distortions of the linear optics, are taken into account as well as synchrotron oscillations. The optimization of the working point is relatively uncritical, as long as the strongest resonances (up to 4th order) are avoided. An ensemle of 16 particles with different initial betatron phases is tracked over 1,000 revolutions (about 2 damping times). The resulting dynamic acceptance for different initial ratios $\epsilon_x/\epsilon_y$ is shown in fig. 3.5.7. It is found to be larger than the linear acceptance, so that the non-linear effects of the sextupoles do not represent a limitation of the acceptance for the injected positron beam. Other nonlinearities can in principle also reduce the acceptance. The effect of the wigglers, with the rather pessimistic assumption of a sinusoidal field shape, is found to be insignificant. We also expect that the effects from multipole errors in the dipoles and quadrupoles can be kept small by proper design and standard manufacturing tolerances.

We conclude the section on the damping ring beam optics by summarizing the main parameters in table 3.5.6.

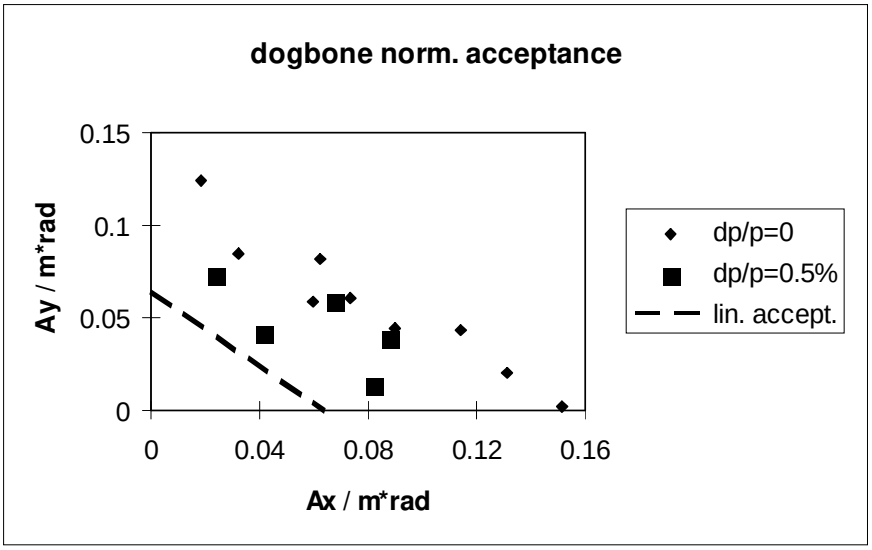


Figure 3.5.7: *Dynamic acceptance of the damping ring. The simulations include a 0.2 mm rms offset of the sextupole magnets.*

### 3.5.4 Rf-System and Collective Effects

According to the design parameters in table 3.5.6 the rf-system has to provide a circumferential voltage of 25 MV and an average power of 1.24 MW to the beam. The choice of frequency, $f_{rf}$=433 MHz, is motivated by having an integer fraction of the main linac frequency and by the availability of high power klystrons. The choice of accelerating cavities has to take into account an analysis of collective effects, in particular coupled bunch instabilities driven by higher order cavity modes (HOM).

#### Cavities and Coupled Bunch Instabilities

We focus here on a concept which uses 4-cell superconducting cavities very similar to the ones installed at HERA (but scaled in frequency from 500 MHz to 433 MHz). Other concepts are also conceivable and will be briefly addressed below.

We assume a power limit per cavity of about 150 kW so that in total 8 cavities are needed. The length of one 4-cell cavity is $4(\lambda_{rf}/2)$=1.39 m and the required accelerating gradient amounts to 2.25 MV/m. From the experience with the HERA-cavities including HOM-couplers, the strongest modes can be estimated to have the following impedances (per 4-cell cavity):

$$Z_{||}(f_{HOM} \approx 0.8\,\mathrm{GHz}) = 60\,rmk\Omega, Z_{\perp} = 13\,\mathrm{M}\Omega/\mathrm{m} \tag{3.5.11}$$

The longitudinal instability growth rate due to higher order modes in the RF system can be calculated as [8]:

$$\frac{1}{\tau_{||}^{k}} = \frac{\alpha I_B f_0}{2(E/e)\nu_s} \sum_{p=-\infty}^{+\infty} (pN_b + k + \nu_s) \cdot Z_{||}(\omega_0(pN_b + k + \nu_s)) \tag{3.5.12}$$

| | |
|---|---|
| Circumference $C$ | 17 km |
| Beam energy $E_b$ | 3.20 GeV |
| # of bunches $n_b$ | 1130 |
| Bunch charge $N_e$ | $3.63 \cdot 10^{10}$ |
| Bunch spacing $\Delta t_b$ | 50 ns |
| Stored current $I_b$ | 116 mA |
| Norm. hor. emittance $\gamma\epsilon_x$ | $1.10 \cdot 10^{-5}$ m |
| Transverse damping time $\tau_{x,y}$ | 33.8 ms |
| Hor./vert. tune $Q_x/Q_y$ | 59.85 / 57.71 |
| Hor./vert. chromaticity $\xi_x/\xi_y$ | -68.6 / -73.3 |
| Norm. acceptance $A_{x,y}$ | 0.06 m |
| Energy loss p. turn $U_0$ | 10.7 MV |
| RF-frequency $f_{RF}$ | 433 MHz |
| RF-voltage $U_{RF}$ | 25 MV |
| Energy spread $\sigma_E$ | 0.10 % |
| Compaction factor $\alpha_c$ | $3.4 \cdot 10^{-4}$ |
| Bunch length $\sigma_z$ | 9.5 mm |
| Synchrotron tune $Q_s$ | 0.095 |
| Energy acceptance $\Delta E_{max}/E$ | 1.5 % |
| Incoh. Space Charge $\Delta Q_y$ | -0.17 |

Table 3.5.6: *Main design parameters of the positron damping ring.*

The upper limit of the growth rate is obtained for that multibunch mode with a frequency coinciding with the mode frequency of the strongest HOM. Using 3.5.11 and scaling the impedance linearly with the number of cavities, we find $\tau_{||}^{-1} = 272\,s^{-1}$. Since the damping rate from synchrotron radiation is only $60\,s^{-1}$, a feedback system is required. The systems installed in PETRA and HERA [9] work with a bunch spacing of 96 ns and provide a damping rate above 1 kHz. It is expected that a similar longitudinal feedback for the damping ring with twice the bandwidth but only about one third the damping rate of the PETRA/HERA systems can be built without problems.

For beam loading compensation, the cavity resonance frequency has to be detuned by several kHz. This can give rise to an instability of the multibunch mode nearest in frequency, with a rise time potentially smaller than the other HOM-driven modes. To avoid this, a simple feedback loop (like the "nearby-mode" feedback in HERA) is foreseen.

In the transverse plane, the instability growth rate is given by [8]:

$$\frac{1}{\tau_\perp^k} = \frac{I_B f_0}{(E/e)} \sum_{p=-\infty}^{+\infty} \beta \mathtt{Re} Z_\perp(\omega_0(pN_b + k + \nu_\perp)) \qquad (3.5.13)$$

With $\beta$=10 m at the cavities and an impedance of $8 \times 13\,\mathrm{M}\Omega$ for the strongest mode, the growth rate is $\tau_\perp = 648\,s^{-1}$, to be compared with a damping rate of $29\,s^{-1}$. The multibunch feedback system in PETRA and HERA is capable of providing a damping

rate of several kHz. With a similar system for the damping ring, suppression of HOM-driven transverse instabilities is guaranteed.

In the transverse plane, coupled bunch instabilities are also strongly driven by the resistive wall effect of the vacuum chamber. The transverse resistive wall impedance of the Al vacuum chamber of the ring yields $\beta \mathtt{Re} Z_\perp[M\Omega] \approx 1300/\sqrt{n}$ (dominated by the straight sections, with about 10% contribution from the wiggler and the arc sections).

The maximum growth rate occurs at the mode number which is equal to the integer part of the tune $k = [\nu_\perp]$, thus, to derive the impedance one should replace $\sqrt{n}$ by the square root of the fractional part of the transverse tune $\sqrt{\Delta\nu_\perp}$. Taking $\Delta\nu_\perp = 0.15$, we get $\tau_\perp^{-1} \approx 2000\ s^{-1}$ for the 17 km long "dog-bone" ring. This instability is much easier to damp than the one driven by the cavity-HOMs, because it requires only a rather low-bandwidth feedback. It is conceivable, though, that a broad-band feedback can be made strong enough to damp the instability driven by the resistive-wall effect as well so that an additional system may not be necessary.

With different concepts for the RF-cavities, a stronger suppression of HOMs is possible. Using about 40 single-cell Cu-resonators of the type foreseen for the PEP-II B-factory, the HOM impedance [10] could be reduced by roughly a factor of two in the longitudinal plane and a factor of five in the transverse plane. Feedback systems are still required, but with relaxed damping rates. As yet another alternative, strongly HOM-damped superconducting single-cell cavities similar to the one tested at CESR [11] could be employed. In that case, the Q-values of the HOMs may be as low as 100 and a broadband feedback could become obsolete, at least in the longitudinal plane.

### Single Bunch Effects

In the longitudinal plane, the microwave instability sets a constraint on the maximum tolerable effective broadband impedance [8]:

$$\Big(\frac{Z_\parallel}{n}\Big)_{eff}^{thr} = \frac{(2\pi)^{3/2}\alpha_c (E/e)\sigma_E^2 \sigma_z}{eN_e c}, \tag{3.5.14}$$

For parameters of the dogbone damping ring we get

$$\Big(\frac{Z_\parallel}{n}\Big)_{eff}^{thr} = 86 m\Omega. \tag{3.5.15}$$

The purely inductive part of the impedance $Z_\parallel^{ind} = -i\omega L$ does not contribute to the microwave instability but still can give rise to bunch lengthening, which is approximately given by [10]:

$$\frac{\Delta\sigma_z}{\sigma_z} \approx \frac{L}{2\sqrt{2\pi}\sigma_z}\frac{N_e r_e}{C\alpha_c \gamma \sigma_E^2}. \tag{3.5.16}$$

An estimate of the different contributions to the broadband impedance is given in ref. [12]. We only summarize the results here, shown in table 3.5.7. The microwave instability is safely avoided (by an order of magnitude) and the inductive part of the impedance is expected to cause a bunch lengthening of about 10%.

| Component | $Z/n$, m$\Omega$ | $k_{loss}$, V/pC |
|---|---|---|
| RF Cavities | 2.3 | 22.0 |
| Resistive wall | 5.1 | 6.5 |
| Total non-inductive | 7.4 | |
| Bellows | 7.8 | 2.8 |
| BPMs | 4.3 | 0.8 |
| Kickers | 1.3 | 2.8 |
| Other induct. | $\sim 4$ | $\sim$2 |
| Total inductive | $\simeq 17$ | |
| Loss factor | | $\simeq$38 |
| Loss power, kW | | $\simeq$25 |

Table 3.5.7: *Contributions to the non-inductive and purely inductive part of the longitudinal broadband impedance according to the estimate given in ref. [12].*

The transverse broadband impedance has also been estimated in ref. [12]. It is found that the mode-coupling instability is not an issue of concern for the damping ring.

### 3.5.5 Injection and Extraction System

Injection into and extraction from the damping ring has to be done bunch-by-bunch in order to cope with the different bunch spacing in the linac and in the ring. This means that the full pulse length of the kicker device must be smaller than twice the bunch spacing in the ring ( $\Delta t_b$(ring)=50 ns for the reference design and 25 ns for the upgrade options). Furthermore, a burst of $n_b$=1130 pulses spaced by $\Delta t_b$(linac)=708 ns has to be provided per injection (extraction) cycle. Assuming that the kickers and septa are installed in the straight section where the beta-function is large ($\approx$150 m), the required kick angle for beam injection with 3 standard deviations clearence at the septum bar is 0.6 mrad (the requirement for extraction is much relaxed due to the smaller beam emittance). This corresponds to a field integral of 0.006 Tm.

The technical solution for the kicker is based on a travelling wave stripline device (see ref. [13]). The effective field integral during the flat top of the pulse (see Fig. 3.5.8) is equal to $2e\hat{U}l/a$ where $\hat{U}$ is the applied voltage, $l$ the kicker length and $a$ the half-aperture. With $\hat{U}$=5 kV, $a$=50 mm and $l$=0.5 m, a single kicker provides a deflection strength of $3 \cdot 10^{-4}$ Tm, so that 20 of these devices are required for the extraction system. A prototype kicker has been built and tested using a high voltage burst pulser and it was shown that an effective pulse length as short as about 10 ns could be achieved [13]. With this approach, a sufficient safety margin allowing for further reduction of the bunch spacing is thus provided.

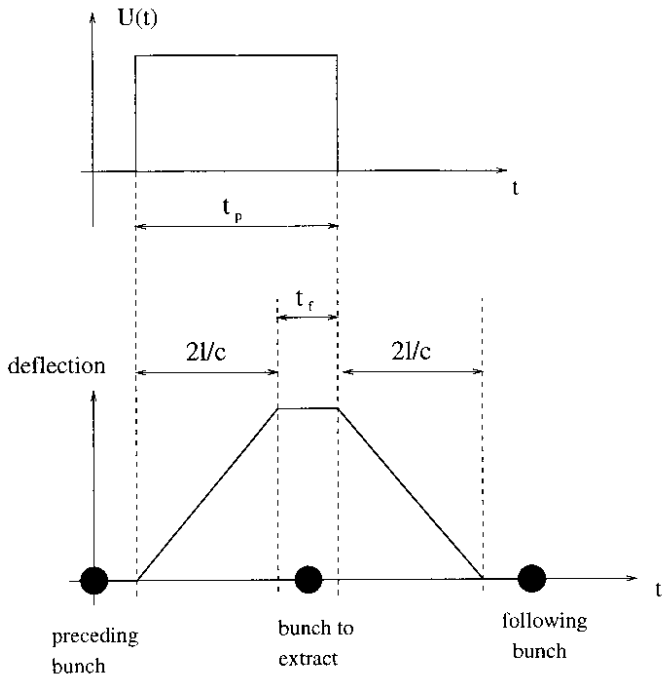


Figure 3.5.8: *Sketch of the travelling wave kicker time structure.*

### 3.5.6 Vacuum System

The vacuum system for the damping ring consists of three parts: two 8 km long straight sections, two arcs and four wiggler sections.

#### Straight Sections

For the straight sections 9.5 m long vacuum chambers will be made from 100 mm diameter aluminum tubes with aluminum CF-flanges welded to the ends. In order to reach the required average pressure of $\bar{p} = 10^{-9}$ mbar titanium sublimation pumps with 1000 l/s are installed every 10 m supplemented with small (60 l/s) ion getter pumps every 20 m. The getter pumps will be also used for pressure read out. The pumps are integrated into 0.3 m long stainless steel chambers with bellows, which are installed between the long aluminum chambers as indicated in fig. 3.5.9. The pump ports and the bellows are rf-shielded by CuBe spring fingers. The flange connection between aluminum-aluminum and aluminum-stainless steel flanges are done by CF-aluminum gaskets.

A third type of chamber is used for the quadrupoles located every 50 m. These 1 m long aluminum or copper coated stainless steel chambers are equipped with beam position monitors (BPM). After mounting them rigidly to the quadrupole, the BPM's will be calibrated with respect to the quadrupole axis. In total 1520 long aluminum chambers, 1520 pump units with bellows and 304 aluminum quadrupole chambers are needed for the straight sections.

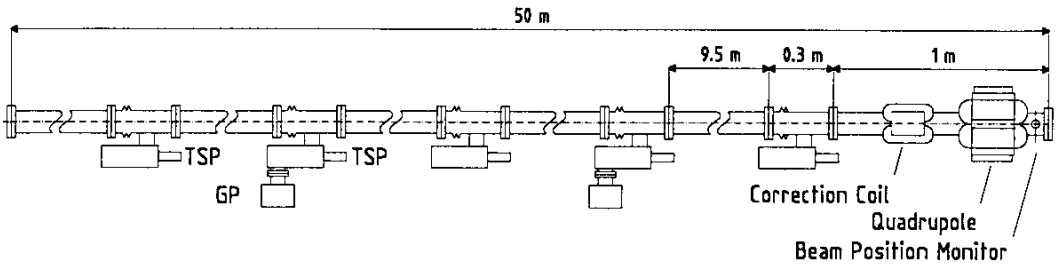


Figure 3.5.9: *Pattern for the vacuum chambers in the straight sections of the TESLA damping ring.*

Pneumatic valves with rf-shields segment the straight sections into several long vacuum sectors. To start pumping and for leak check manual valves are foreseen at some of the ion getter pumps to connect movable pump stations.

The vacuum chamber in each 8.5 m arc cell is split in the following way: two long chambers passing the dipole magnet and the correction coil and two short chambers through the quadrupole and sextupole magnets. All chambers will have the same elliptical aperture of $52 \times 28\,\mathrm{mm}^2$. The arrangement of the vacuum chambers is shown in fig 3.5.10.

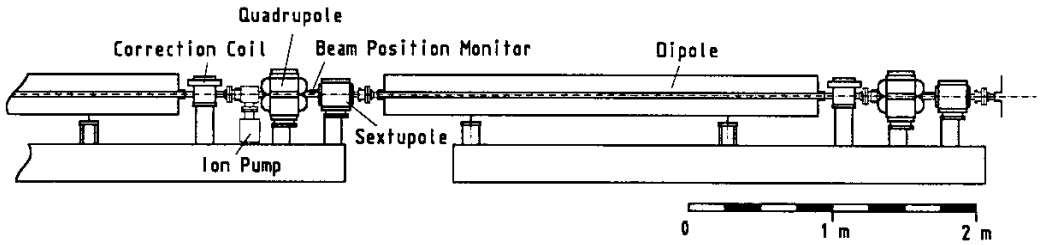


Figure 3.5.10: *Arrangement of the vacuum chambers in the arcs of the damping ring.*

The required vacuum of $p = 10^{-8}$ mbar for the arcs is somewhat less stringent than in the straight sections. However, due to the synchrotron radiation of 170 W/m the gas load from desorption of gas molecules from the chamber walls will be much higher. Therefore the aluminum vacuum chamber in the 3 m long dipole magnets has a separate channel for integrated pumps, e.g. NonEvaporable Getter (NEG) vacuum pumps. Fig. 3.5.11 shows a tentative layout of the profile of this chamber including a channel for water cooling. The chamber will be made by extrusion and bent according to the bending radius of the dipole. The integrated pumps are mounted on a support, which also serves as rf-shield of the pump channel as indicated in fig. 3.5.11. This structure will be slid into the aluminum chamber. The pump channel is terminated on both sides of the dipole magnet. Straight elliptical aluminum tubes with transition into

round aluminum CF-flanges are welded on both sides. The water channel is bridged between two dipole magnets.

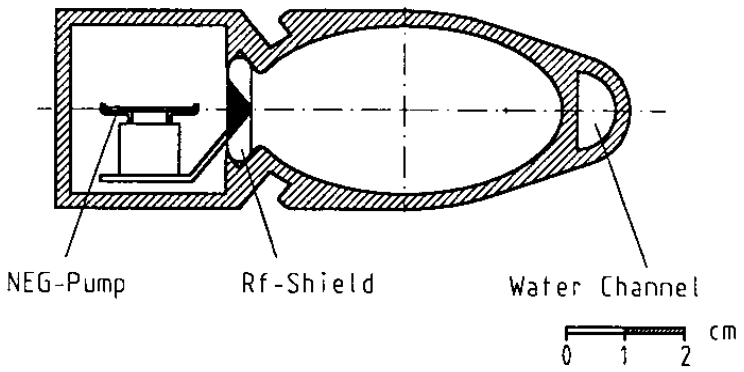


Figure 3.5.11: *Tentative layout of the vacuum chamber through the dipole magnets in the arcs of the damping ring. Integrated pumps are installed in a separate pump channel. The chamber is water cooled.*

Each quadrupole must be equipped with a BPM. Therefore short straight stainless steel or copper chambers of the same elliptical profile as the other chambers, formed by pressing of a tube, are rigidly mounted in the quadrupoles. The BPM's will be calibrated with respect to the quadrupole axis. Bellows are integrated into these chambers on both sides of the quadrupoles. Small ion getter pumps (60 l/s) attached to pump ports in every second unit supplement the integrated pumps. As in the straight sections rf-shielding of the bellows and pump ports is done by CuBe spring fingers. In case of a stainless steel chamber the remaining part of the pipe will be copper coated.

The magnets and vacuum chambers of each half cell are mounted on one girder, prealigned and installed as one unit in the tunnel for the arcs.

In each arc one pneumatic valves with rf-shield will split the vacuum system into two 200 m long sectors to facilitate activation and regeneration of the NEG pumps. Movable pump stations can be connected through manual valves attached to some ion getter pumps to start pumping.

### Wiggler Sections

The four wiggler sections are each 120 m long. The vacuum chamber in each 10.5 m wiggler cell is split into 4 m long chambers through the wiggler magnets and 1 m long chambers through the quadrupole magnets and correction coils. About 15 kW of synchrotron radiation will be deposited in the vacuum chamber of each half cell.

The aluminum chamber through the wiggler magnets has a beam chamber with vertical aperture of about 20 mm and an antechamber on either side with a slot height of 25 mm as shown in fig. 3.5.12. Vacuum pumping will be performed by NEG pumps

located at the end of each slot. The antechamber slots are sloped to protect the pumps against direct synchrotron radiation. The chamber will be water cooled .

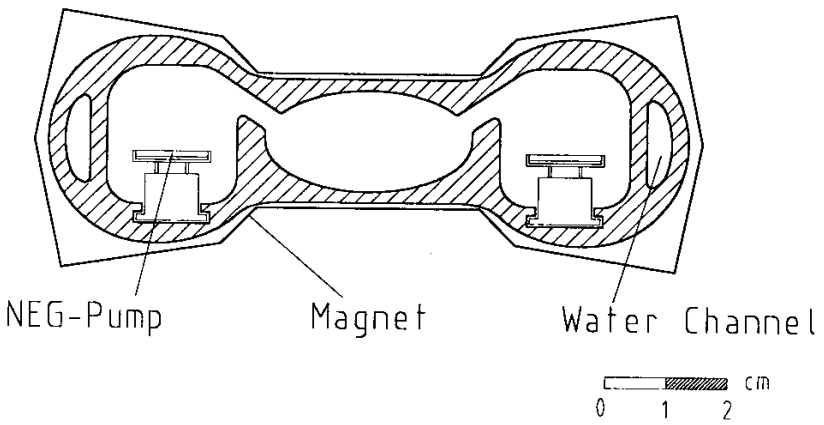


Figure 3.5.12: *Schematic of the cross section of the wiggler vacuum chamber for the damping ring.*

The vacuum chamber through the correction coil and the quadrupole magnet is equipped with BPM's, bellows and a small ion getter pumps (60 l/s) in every second unit to supplement the integrated pumps. Again, rf-shielding of the bellows and pump ports will be done by CuBe spring fingers. In front of the quadrupole magnets absorbers are needed to shield the synchrotron radiation. Pneumatic valves on both sides of each wiggler will separate the wiggler vacuum from the arcs and straight sections.

# Bibliography

[1] B. Autin and Y. Marti, *Closed Orbit Correction in A.G. Machines Using a Small Number of Magnets*, CERN-ISR-MA-73-17, 1973.

[2] E. Gianfelice et al., *Application of a Beam-Based Alignment Technique for Optimizing the Electron Spin Polarization at HERA*, Proc. 5th Europ. Part. Acc. Conf., Barcelona 1996.

[3] R. Brinkmann and J. Roßbach, *Observation of Closed Orbit Drift at HERA Covering 8 Decades of Frequency*, Nucl. Instr. Meth. A350, p. 8, 1994.

[4] T. O. Raubenheimer, *The Generation and Acceleration of Low Emittance Flat Beams for Future Linear Colliders*, Thesis, SLAC-387, 1991.

[5] T. O. Raubenheimer, *Emittance Growth due to Beam-Gas Scattering*, KEK report 92-7, 1992.

[6] A. Piwinski, *Intrabeam Scattering with Vertical Dispersion*, Proc. SSC Workshop, Ann Arbor, MI, 1983.

[7] H. Wiedemann, *Low Emittance Storage Ring Design*, Proc. US/CERN Part. Acc. School, South Padre Island, TX, 1986.

[8] A. Chao, *Physics of Collective Beam Instabilities in High Energy Accelerators*, John Wiley & Sons, Inc., 1993.

[9] M. Ebert et al., *Transverse and Longitudinal Multi-Bunch Feedback Systems for PETRA*, DESY-91-036, 1991.

[10] S. Heifets et al., *Impedance Study for the PEP-II B-Factory*, SLAC/AP-99, 1995.

[11] S. Belomestnykh et al., *Wakefields and HOMs Studies of a Superconducting Cavity Module with the CESR Beam*, IEEE Proc. Part. Acc. Conf., Vol. 5, p. 3391, Dallas 1995.

[12] V. Shiltsev, *Beam Dynamics Issues in the TESLA Damping Ring*, DESY-TESLA-96-02, 1996.

[13] B.I. Grishanov, F.V. Podgorny, J. Rümmler and V.D. Shiltsev, *Very Fast Kicker for Accelerator Applications*, DESY-TESLA-96-11, 1996.